Supplementary Information

Capacitive Versus Diffusion Controlled Mechanism in Mesoporous Cobalt Hexacyanoferrate/Carbon Composite for High-Performance Capacitive Deionization Device-Electrochemical Quartz Crystal Microbalance (EQCM) Studies

Mahima S [a], Dasari Hindu Bhavani [a], Mahesh Padaki [b], Srinivasa Budagumpi[b], D H Nagaraju [a*]

[a] Department of Chemistry, School of Applied Sciences, REVA University, Yelahanka, Bengaluru, Karnataka, 560064, India.

[b] Centre for Nano and Material Sciences, JAIN (Deemed–to–be University), Jain Global Campus, Kanakapura, Ramanagaram, Bangalore 562112, India

* Corresponding Author: Department of Chemistry, School of Applied Sciences, REVA University, Yelahanka, Bengaluru, Karnataka, 560064, India.

E-mail: dhnagu@gmail.com. Tel: +91 9900634435

Table S1 X-ray photoelectron spectroscopy (XPS) analysis showing the atomic percentage of C 1s, N 1s, O 1s, Fe 2p1, Co 2p1 of CoHCF and Meso-CoHCF.

CoHCF		Meso-CoHCF	
Name	Atomic %	Name	Atomic %
C 1s	57.85	C 1s	56.42
N 1s	24.24	N 1s	26.69
O 1s	13.35	O 1s	10.21
Fe 2p1	2.92	Fe 2p1	3.43
Co 2p1	1.64	Co 2p1	3.25

The surface atomic percentages listed in Table S1 were obtained from XPS analysis and therefore represent the elemental composition of only the outermost layers of the material. The theoretical atomic percentages for $Co[Fe(CN)_6]$ (7.14 at% Co, 7.14 at% Fe, 42.86 at% C and 42.86 at% N) indeed represent the ideal bulk stoichiometry of a defect-free, fully occupied Prussian blue analogue (PBA) unit cell. However, experimentally measured atomic percentages, such as those obtained from X-ray photoelectron spectroscopy (XPS), frequently differ from these ideal values for several well-documented reasons in PBA materials. PBAs typically exhibit intrinsic hexacyanometallate vacancies, coordinated/interstitial water molecules and a range of surface terminations, all of which alter the local atomic environment and elemental distribution compared to the idealized formula. Furthermore, XPS is a surface-sensitive technique (~5–10 nm sampling depth) and predominantly probes the outermost atomic layers, which often have different composition from the bulk due to surface relaxation, defect enrichment and adsorbed species. As a result, surface atomic percentages determined by XPS can deviate significantly from the bulk stoichiometric expectations. Similar discrepancies have been reported and rationalized in prior PBA studies, where measured elemental differed from nominal compositions due to vacancies, hydration and synthesis-dependent structural variation [1,2].

Additionally, the comparatively low Co and Fe atomic percentages and the elevated C 1s content observed in Table S1 arise from both the intrinsic CN-rich framework of PBAs. The PBA structure inherently contains a high proportion of carbon and nitrogen because each Fe center is coordinated by six cyanide (–C≡N) ligands, resulting in a much larger number of C and N atoms relative to metal centers [3]. The carbon signal is further enhanced by adventitious carbon adsorption from ambient exposure and the use of conductive carbon tape during sample mounting, both of which are known to increase the C 1s contribution in XPS spectra [4]. This effect becomes more pronounced in meso-CoHCF due to its higher surface area, which promotes adsorption of carbon-containing species. Supporting this interpretation, EDX analysis, although bulk-sensitive, also shows dominant C and N signals; however, EDX is semi-quantitative and less reliable for light elements, often leading to their apparent overestimation.

Figure S1

The Figure S1a and d shows the survey spectrum of CoHCF and meso-CoHCF respectively, confirming the successful formation of cobalt hexacyanoferrate. The spectrum clearly exhibits Co 2p, Fe 2p, C 1s, N 1s, and O 1s signals, with no impurity peaks, indicating good compositional purity. In Carbon spectra of both materials, the peak at 284.60 eV arises from adventitious C–C/C–H species and the peak near 286.02 eV corresponds to the cyanide carbon (C≡N) of the PBA framework as show in Fig S1b. These are intrinsic to the structure and appear in both samples. However, a distinct peak at 288.72 eV is observed only in meso-CoHCF Figure S1e. This peak is assigned to the N–C=O carbonyl carbon of PVP. Since this carbon is bonded to both nitrogen and oxygen, it exhibits a large shift to higher binding energy. This carbon environment chemically requires a corresponding nitrogen signal in N 1s and an oxygen signal in O 1s, which are indeed observed at 399.36 eV and 531.66 eV, respectively, confirming the presence of residual PVP only in meso-CoHCF.

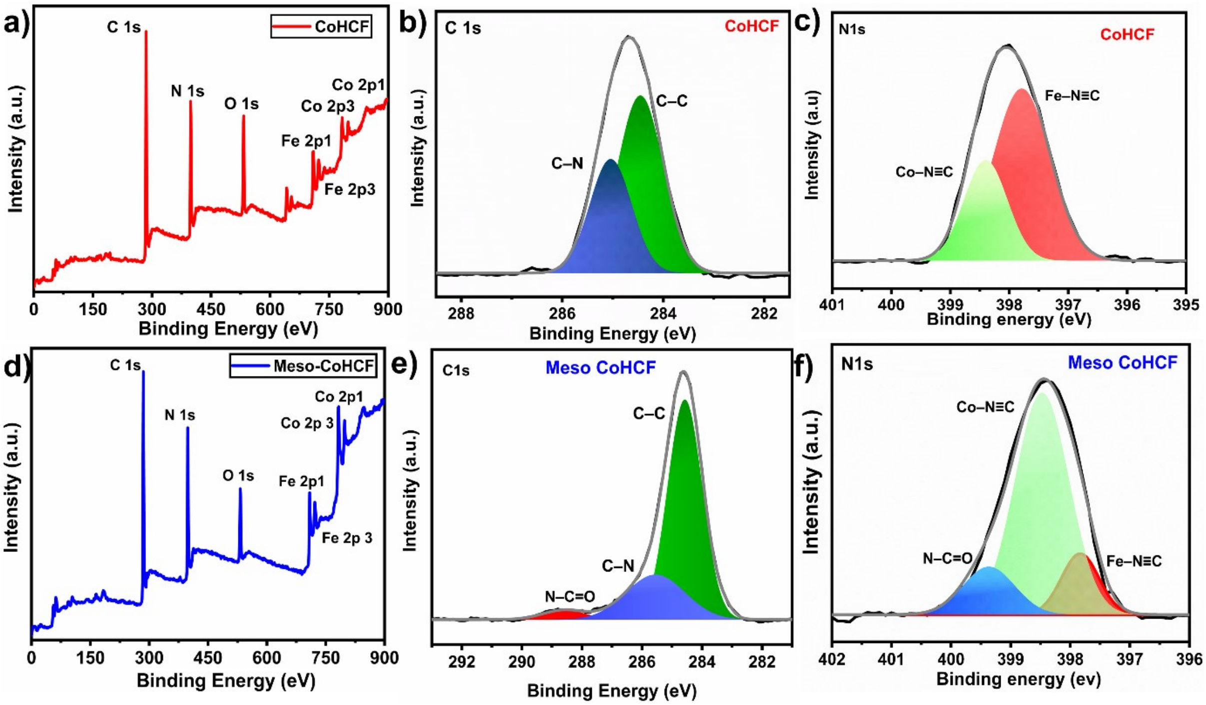

Figure S1 a) Survey spectra b) Carbon spectra c) Nitrogen spectra of CoHCF and d) Survey spectra e) Carbon spectra f) Nitrogen spectra of meso-CoHCF.

The high-resolution N 1s spectra of both CoHCF (Fig S1c) and meso-CoHCF (Fig S1f) exhibit two main peaks centered at 397.81 eV and 398.42 eV. The peak at 397.8 eV corresponds to the cyanide nitrogen in the Fe–N≡C bond, i.e., nitrogen directly coordinated to Fe within the Co–N≡C–Fe framework. The peak at 398.4 eV is attributed to nitrogen in the Co–N≡C bond and to cyanide nitrogen located near intrinsic [Fe(CN)$_6$] vacancy sites. These two peaks are characteristic signatures of the PBA lattice and are common to both materials. An additional peak at 399.36 eV is observed only in meso-CoHCF which is assigned to the lactam nitrogen (>N–C=O) of residual PVP as shown in Figure S1e. This binding energy range is well established for PVP nitrogen (399.2–400.5 eV) and is absent in CoHCF, confirming that PVP residue is present only in meso-CoHCF.

Figure S2

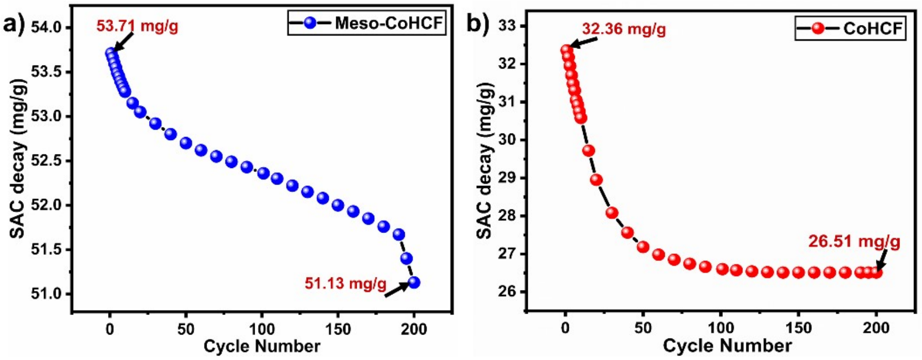

Figure S2: SAC decay curve of a) meso-CoHCF and b) CoHCF

The long-term operational stability of the electrodes was systematically evaluated over 200 consecutive CDI adsorption–desorption cycles using asymmetric electrodes in the CDI cell. The salt adsorption capacity (SAC) was calculated using the standard relation Eq. (5) depicted in the revised manuscript:

For meso-CoHCF, the SAC decreased only slightly from 53.71 to 51.13 mg/g after 200 cycles as shown in Figure S2a, giving a retention of:

$$\frac{51.13}{53.71} \times 100 = 95.2\ \%$$

The very marginal decline demonstrates the excellent structural robustness of the mesoporous framework, highly reversible ion adsorption/desorption behavior, and minimal pore obstruction or surface fouling during prolonged operation.

In contrast, CoHCF, the initial SAC of 32.36 mg/g decreased to 26.51 mg/g after 200 cycles as shown in Figure S2b, corresponding to a retention of:

$$\frac{26.51}{32.36} \times 100 = 81.9\ \%$$

The noticeable and non-linear decay in SAC during cycling indicates progressive pore blockage, ion trapping and structural instability arising from the low surface area and irregular, non-mesoporous morphology of CoHCF. This clear difference in SAC retention directly highlights the critical role of mesoporosity, higher surface area and uniform morphology in ensuring long-term CDI durability and validates the superior practical suitability of the mesoporous electrode for desalination applications.

Table S2: Comparison of CDI Performance Metrics of Reported Electrode Materials under Different Operating Conditions.

Sl No	**Materials**	**CDI Mode**	**Flow rate mL/min**	**Voltage**	**NaCl in ppm**	**SAC (mg/g)**	**ASAR (mg/g/min)**	**EC (kWh/kg)**	**Ref**
1	Ni-Cu PBA/CNT	HCDI	20	1.2	500	41.25	5.2	0.108	5
2	PB/PANI	MCDI	50	1.2	500	59.2	0.58	1	6
3	NiHCF@3DC-2	HCDI	-	0.8	20000	47.8	11.00	0.44	7
4	Co-Ni-PBA@MXene	HCDI	20	1.2	500	60.2	10	0.283	8
5	MnPBA	HCDI	5	1	1000	10.92	-	0.8	9
6	CoHCF/PANI	HCDI	4.6	1.4	500	30.48	3.66	0.92	10
7	FeHCF@NiHCF	CDI	20	1.2	2000	74.15	18.01	0.65	11
8	NiCoFe-PBA	HCDI	10	1.2	500	63.18	1.05	0.27	12
9	FePBA	HCDI	5	1	Mixed solution	54.8	0.69	0.26	13
10	PB/CNF	CDI	35	1.4	500	51.81	0.8	0.81	14
11	CoHCF	HCDI	10	1.2	500	46.22	1.54	1.3	This work
12	Meso-CoHCF	HCDI	10	1.2	500	64.31	2.14	0.55	This work

References:

Supplementary Information

1 H. L. B. Boström, I. E. Collings, D. Daisenberger, C. J. Ridley, N. P. Funnell and A. B. Cairns, *J. Am. Chem. Soc.*, 2021, **143**, 3544–3554.

2 J. Cattermull, M. Pasta and A. L. Goodwin, .

3 P. M. Frías-Ureña, M. Bárcena-Soto, V. Soto, K. Chávez, E. Orozco-Guareño, J. Badillo-Camacho, J. R. Robledo-Ortiz, I. Fernández-Cervantes and S. Gómez-Salazar, *ACS Omega*, 2025, **10**, 11421–11438.

4 Y. Xiao, J. Xiao, H. Zhao, J. Li, G. Zhang, D. Zhang, X. Guo, H. Gao, Y. Wang, J. Chen, G. Wang and H. Liu, *John Wiley and Sons Inc*, 2024, preprint, DOI: 10.1002/smll.202401957.

5 J. Guo, Y. Wang, Y. Cai, H. Zhang, Y. Li and D. Liu, *Desalination*, DOI:10.1016/j.desal.2022.115622.

6 W. Shi, X. Liu, T. Deng, S. Huang, M. Ding, X. Miao, C. Zhu, Y. Zhu, W. Liu, F. Wu, C. Gao, S. W. Yang, H. Y. Yang, J. Shen and X. Cao, *Advanced Materials*, DOI:10.1002/adma.201907404.

7 S. Wang, G. Wang, Y. Wang, H. Song, S. Lv, T. Li and C. Li, *ACS Appl. Mater. Interfaces*, 2020, **12**, 44049–44057.

8 Y. Cai, W. Zhang, J. Zhao and Y. Wang, *Appl. Surf. Sci.*, DOI:10.1016/j.apsusc.2023.156926.

9 X. Zhang, E. A. Toledo-Carrillo, D. Yu and J. Dutta, *ACS Applied Materials and Interfaces* , 2022, **14**, 40371–40381.

10 D. Ma, X. Xue, M. Niu, Y. Wang, Q. Luo, X. Zhu, H. Li and D. Wang, *Sep. Purif. Technol.*, DOI:10.1016/j.seppur.2024.127804.

11 Z. Fan, W. Wang, J. Ren, R. P. Ren and Y. K. Lv, *J. Environ. Chem. Eng.*, DOI:10.1016/j.jece.2025.119779.

12 J. Hu, Q. Han, Y. Liu, Y. Fan, W. Xi, Y. Zhang, R. Wang, H. Wang, Y. Gong and J. Jin, *Appl. Surf. Sci.*, DOI:10.1016/j.apsusc.2025.164854.

13 D. Kim, H. Lee and S. Jeon, *Desalination*, DOI:10.1016/j.desal.2025.119487.

14 X. Wang, Q. Ma, L. Wang, D. Jia, C. Leng, M. Xu, N. Guo, L. Ai and X. Gong, *ACS Appl. Nano Mater.*, 2024, **7**, 12970–12979.